Geophysical Research Letters

RESEARCH LETTER
10.1029/2020GL090997

Three Regimes of Temperature Distribution Change Over Dry Land, Moist Land, and Oceanic Surfaces

Suqin Q. Duan[1], **Kirsten L. Findell**[2], **and Jonathon S. Wright**[3]

[1]Program in Atmospheric and Oceanic Sciences, Princeton University, Princeton, NJ, USA, [2]NOAA/Geophysical Fluid Dynamics Laboratory, Princeton, NJ, USA, [3]Department of Earth System Science, Tsinghua University, Beijing, China

Key Points:

- Dry land, moist land, and oceanic surfaces experience different changes in summertime mean and extreme temperatures
- Moist land surfaces feature larger warming in extreme-relative-to-mean temperatures, while dry surfaces warm more in the mean
- Amplified warming in extreme temperatures is attributed to suppressed evapotranspiration and larger Bowen ratios

Supporting Information:

- Supporting Information S1

Correspondence to:
S. Q. Duan,
sduan@princeton.edu

Citation:
Duan, S. Q., Findell, K. L., & Wright, J. S. (2020). Three regimes of temperature distribution change over dry land, moist land, and oceanic surfaces. *Geophysical Research Letters*, *47*, e2020GL090997. https://doi.org/10.1029/2020GL090997

Received 28 SEP 2020
Accepted 23 NOV 2020

© 2020. American Geophysical Union. All Rights Reserved.

Abstract Climate model simulations project different regimes of summertime temperature distribution changes under a quadrupling of CO_2 for dry land, moist land, and oceanic surfaces. The entire temperature distribution shifts over dry land surfaces, while moist land surfaces feature an elongated upper tail of the distribution, with extremes increasing more than the corresponding means by ~20% of the global mean warming. Oceanic surfaces show weaker warming relative to land surfaces, with no significant elongation of the upper tail. Dry land surfaces show little change in turbulent sensible (SH) or latent (LH) fluxes, with new balance reached with compensating adjustments among downwelling and upwelling radiative fluxes. By contrast, moist land surfaces show enhanced partitioning of turbulent flux toward SH, while oceanic surfaces show enhanced partitioning toward LH. Amplified warming of extreme temperatures over moist land surfaces is attributed to suppressed evapotranspiration and larger Bowen ratios.

1. Introduction

Extreme heat events threaten the well-being of both the built and natural world. It is therefore important to study how these events will change under global warming. Changes in temperature extremes have been studied at scales ranging from local to global (e.g., Diffenbaugh & Ashfaq, 2010; Fischer & Schär, 2009; Hansen et al., 2012; Tingley & Huybers, 2013). Many of these studies have compared past temperature probability (or frequency) distribution functions (PDFs) with recent or projected future PDFs, focusing especially on changes in the likelihood of extreme heat events (e.g., Diffenbaugh & Ashfaq, 2010; Diffenbaugh & Charland, 2016; Diffenbaugh & Scherer, 2011; Fischer et al., 2013; Hansen et al., 2012; Wang et al., 2015). The consensus emerging from these studies is that extreme temperature events will occur more often and become (on average) more extreme. However, it is often unclear whether and to what extent these changes arise from shifts in the distribution mean relative to changes in the distribution shape.

Despite robust conclusions that mean state warming contributes to the increased likelihood of extreme heat events over the historical period and/or in future projections (e.g., Diffenbaugh et al., 2017; Donat & Alexander, 2012; McKinnon et al., 2016), some (especially regional) studies have reported that changes in variability and/or higher-order statistical moments are critical for changes in the occurrence frequency of record-breaking heat events (e.g., Ballester et al., 2010; Chan et al., 2020; Della-Marta et al., 2007; Kodra & Ganguly, 2014; Schär et al., 2004), whereas other studies have argued that changes in higher-order moments are generally insignificant, or inconsistent (e.g., Donat & Alexander, 2012; Gross et al., 2018; McKinnon et al., 2016; Rhines & Huybers, 2013). The global spatial distribution of changes in the warm tail in relation to changes in the mean is even less conclusive. Local metrics for both the tail and the mean of the distribution are required to fully reveal changes in the local asymmetry, and comparing annual-maximum daily maximum temperature to the global mean temperature (instead of the local mean) does not reveal changes in the local distribution shape (e.g., Vogel et al., 2017).

Several factors complicate interpretation of existing results and understanding of future changes in the temperature distribution shape. First, the temperature distribution varies across different time scales and temperature metrics (e.g., Sulikowska & Wypych, 2020). It is difficult to reconcile results based on annual means (e.g., Diffenbaugh & Charland, 2016; Diffenbaugh & Scherer, 2011) with those based on seasonal means (e.g., Wang et al., 2015), or annual-maximum daily means or maxima (e.g., Diffenbaugh & Charland, 2016; Donat et al., 2017). Changes in the distribution shape may likewise differ by season (e.g., Chan

et al., 2020; Rhines et al., 2017). Second, the use of aggregated samples, regional averages, or individual grid cells when constructing percentiles can also impact the results and their interpretation. Third, some studies have used multidecadal time series from the Representative Concentration Pathway and/or historical observations to calculate and compare distributions without removing trends (e.g., Hansen et al., 2012; Kodra & Ganguly, 2014). This may introduce biases in the variability because trends in the mean state contribute to the spread in a multiyear PDF (Rhines & Huybers, 2013; see also Della-Marta et al., 2007, their Figure 3). Moreover, sampling the upper percentiles of all summer days spanning decades (e.g., Clark et al., 2006) is likely to make the sampled days dominated by the warmest part of the seasonal cycle. Interpretation of changes in the shapes of PDFs constructed this way may be complicated by changes in the seasonal cycle.

Considering these factors, we focus on the summer season, when the potential for heat waves to bring lethal health or agricultural impacts is greatest. We use daily data and construct our methodology to avoid sampling only the hottest part of the seasonal cycle (see Section 2.2 for details). We also use outputs from piControl simulations and the equilibrated stages of abrupt-4 × CO_2 experiments to avoid artificial broadening of the distributions due to trends in the mean state.

We investigate how the hottest summertime temperatures change relative to summer-mean temperatures at each location on the globe, which measures how extreme temperatures at each location evolve due to changes in the distribution "shape." We compare spatial patterns of this "shape effect" and the summertime mean change, and find that the characteristic features can be jointly linked to local surface properties. These results are reported in Section 3.1. We further assess how underlying surface fluxes change over different surface conditions, paying particular attention to changes in evapotranspiration (Sections 3.2 and 3.3). We summarize and discuss the results in Sections 4 and 5.

2. Data and Methodology

2.1. Model Outputs

We use the Climate Model Intercomparison Project Phase 5 (CMIP5) model outputs to analyze projected changes in temperature distribution. Specifically, we take daily output from the preindustrial control (piControl) experiment as the unperturbed state and contrast it against daily output from simulations subjected to an abrupt quadrupling of CO_2 (abrupt-4 × CO_2; 4 × CO_2 for short) as the warmed state (see Taylor et al., 2012, for details of experiment design). We use only the last 50 years from each simulation, after the models have approximately reached equilibrium. We focus on the summer season because of its relevance to heat risk; changes in winter season are influenced by different processes and show different patterns. Here, we define summer as June, July, and August (JJA; 92 days) for all locations in the Northern Hemisphere and December, January, and February (DJF; 90 days) for all locations in the Southern Hemisphere. This definition of summer is an idealization, especially for tropical and subtropical regions where the seasonality of surface air temperature is less pronounced. However, our sampling approach for extreme temperatures (see Section 2.2) is designed to mitigate sensitivity to the seasonal cycle. Interestingly, although the seasonal cycle of mean temperature does not peak in solstice seasons in the tropics, the extreme-relative-to-mean temperature increase (the amplification) does. The reason is related to soil moisture and will be elaborated in a forthcoming paper. For the current paper, we only show results for JJA/DJF.

Our analysis is based on outputs from the seven models that contributed daily values of mean and maximum temperature, surface radiation, and turbulent energy flux outputs for both the piControl and 4 × CO_2 experiments: GFDL-ESM2M, CanESM2, MIROC5, MIROC-ESM, HadGEM2-ES, IPSL-CM5A-MR, and MRI-CGCM3. Multimodel mean results are calculated after re-gridding all model outputs onto a common $2^{\circ} \times 2^{\circ}$ latitude-longitude grid. We considered five additional models that reported daily temperature for both the piControl and 4 × CO_2 experiments but these models did not provide all surface fluxes. The temperature change patterns we isolate do not change with inclusion of these models. Therefore, to maintain consistency with the surface flux quantities, we focus on results for the seven models listed above. Three of these seven models (HadGEM2-ES, MIROC-ESM, and MRI-CGCM3) provided surface energy flux outputs for only 20 years of simulation time, rather than the full 50 years; for these three models our analysis is limited those 20 years.

2.2. Analysis Method

To investigate changes in the summertime temperature distribution, we examine changes in the mean and changes in the upper tail relative to the mean. For mean warming, we use daily mean surface air temperature (T) and average over all summer days to get summer-mean temperature ($\overline{T}$). We then calculate the difference in $\overline{T}$ between the piControl and $4 \times CO_2$ climatologies ($\Delta\overline{T}$). Here, Δ denotes the difference between the two climate states and the overbar indicates an average over all summer days. Summer-mean changes in other variables are calculated in the same way and reported using similar notation.

For extreme warming relative to mean warming, we examine changes in the upper range of the daily maximum temperature (T_{dmx}), estimated as the difference between the mean of the largest 20% of T_{dmx} ($T_{\mathrm{dmx}}^{\mathrm{top20pct}}$) and the mean of all T_{dmx} values in each climate state. We examine how this spread changes from the control climate to the warm climate (i.e., $\Delta\left(T_{\mathrm{dmx}}^{\mathrm{top20pct}} - \overline{T_{\mathrm{dmx}}}\right)$. This term can be interpreted as the difference in the tail-to-mean spread of T_{dmx} between the two climate states, or, as the change in the warmest T_{dmx} ($\Delta T_{\mathrm{dmx}}^{\mathrm{top20pct}}$) minus the change in the mean T_{dmx} ($\Delta\overline{T_{\mathrm{dmx}}}$). A positive value indicates a stretching of the upper tail of the distribution (i.e., the hot extreme warms more than the mean). Sensitivity testing on the choice of threshold (top 20%, top 10%, and higher) confirms that our conclusions do not depend on this choice.

The top 20% T_{dmx} in this paper is identified in the following way: for each summer calendar day, we identify the 80th percentile of T_{dmx} among the 50 years (i.e., the warmest 10 years) and average T_{dmx} over those 10 years. The average of these values over all summer days is then designated as $T_{\mathrm{dmx}}^{\mathrm{top20pct}}$. An illustration of the sampling method is shown in the supporting information. This procedure avoids preferential selection of climatologically warmer days within the seasonal cycle and, by extension, limits the confounding influence of changes in the seasonal cycle. Comparisons of this sampling method with those sampling the upper percentiles of all days directly and after removing the mean seasonal cycle are provided in SI. Composites for surface flux variables, including the sensible heat flux (SH), latent heat flux (LH), and radiation fluxes are conditioned on T_{dmx}. This is to say, we sample the same calendar days for these variables as for T_{dmx}.

3. Results

3.1. Contrast of Mean and Extreme Warming

The mean warming pattern (Figure 1a) shows the familiar land-sea warming contrast, with the largest warming over continental regions in the middle- and high-latitude Northern Hemisphere. The extreme-relative-to-the-mean warming pattern (Figure 1c) shows no consistent signal over the ocean but strong positive values (i.e., amplified warming of the warmest temperatures) over tropical and subtropical land. The magnitude of this amplification is as large as 20% of the global mean warming, indicating that global warming is projected to warm the warmest days worst (WWWW). Areas where models robustly project WWWW include the southern United States, western Europe, central and southern Africa, India, Southeast Asia, and South America.

We further bin land grid cells according to the climatological summer-mean Aridity Index (AI) (Gentine et al., 2012; Milly & Dunne, 2016), defined as $0.8\mathrm{R}_{\mathrm{net}} / L_v \mathrm{Pr}$ with $\mathrm{R}_{\mathrm{net}}$ the net (longwave plus shortwave) radiation flux absorbed at the surface, L_v the latent heat of vaporization, and Pr the precipitation. A large AI indicates a dry hydro-climate and a small AI indicates a wet hydro-climate (further details provided in supporting information). Changes in mean and extreme-relative-to-the-mean temperatures are shown as functions of latitude and AI in Figures 1b and 1d. Dry land regions warm more in the mean (Figure 1b). By contrast, moist land regions in the tropics and subtropics are most prone to amplified warming in the extreme-relative-to-the-mean (Figure 1d). Glaciated land in polar regions show less warming in the extreme-relative-to-the-mean, which is related to increased heat flux into the ground on hot days. As there are more complicated ice dynamics and thermodynamics involved in glaciated areas, we exclude these areas from the scope of this paper. An alternative view of temperature changes against AI for all land grid cells within 60°S-60°S is shown in Figure S3.

The results suggest three predominant regimes of summer temperature distribution changes under global warming:

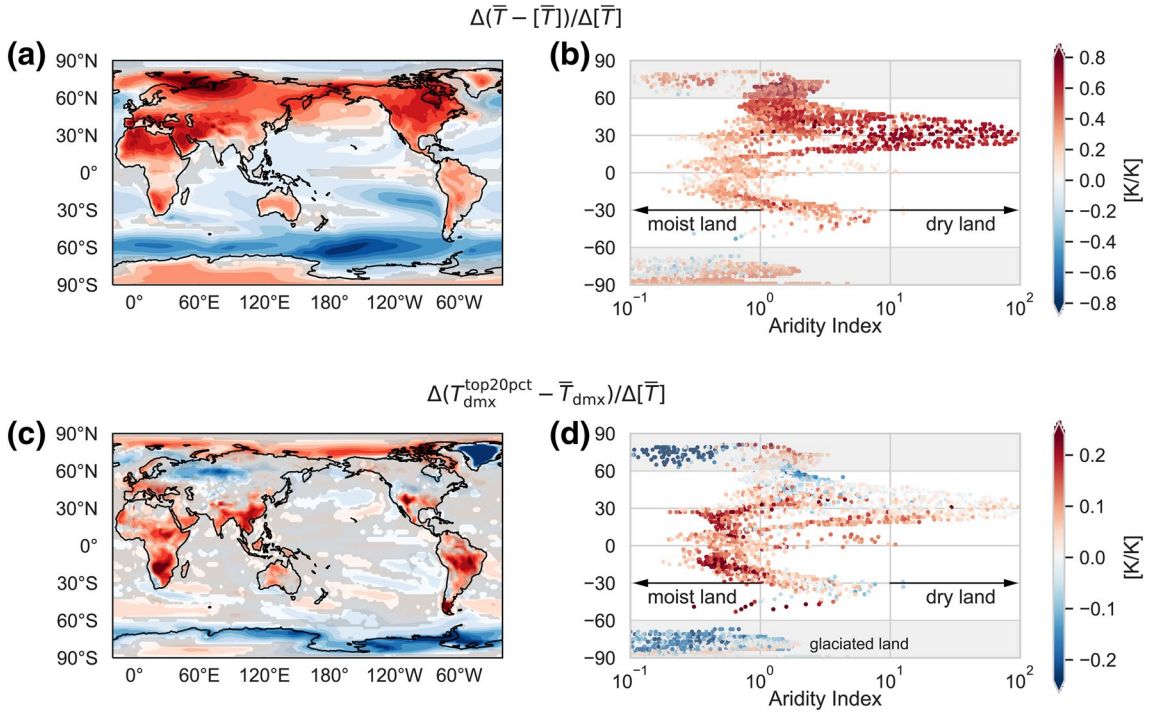

Figure 1. Patterns of multimodel mean changes in selected temperature metrics between the piControl and 4 × CO_2 climates: (a, b) Changes in local summer-mean T relative to global-mean summer-mean T (denoted as $[\overline{T}]$); and (c, d) changes in the warmest local daily maximum temperatures ($T_{dmx}^{top20pct}$) relative to local summer-mean T_{dmx}. Results from each model are normalized by that model's simulated change in $[\overline{T}]$ before averaging to account for differences in climate sensitivity among the models. Locations where fewer than six out of the seven models agree on the sign of the change are masked by gray shadings to emphasize results that are qualitatively robust among the models. (b) and (d) correspond to the spatial distributions in (a) and (c), respectively, with each dot representing a land grid cell. Colors indicate the same fractional temperature changes as in (a) and (c), plotted as a function of latitude and Aridity Index (AI) (defined as $0.8R_{net}$ / L_v Pr; see text in Section 3.1 for details).

- Dry land regions (the dry land regime) show relatively large shifts in mean summer temperature but little amplification of extreme temperatures relative to the mean.
- Oceanic regions (the oceanic regime) show a smaller shift in mean summer temperature. Like the dry land regime, the oceanic regime shows negligible amplification in the shape of the upper tail.
- Moist land regions (the moist land regime) show smaller mean warming compared with dry land regions but significant elongation of the upper tail of the distribution. This regime shows the most pronounced amplification of extreme hot days relative to mean warming.

In the following two subsections, we investigate changes in surface fluxes for these three regimes.

3.2. Warming of the Mean

To better understand the contrasting patterns of mean warming and extreme-day warming in surface air temperature, we start by considering the surface enthalpy budget:

$$c_s\rho_s\frac{\partial T_{sfc}}{\partial t} = R_{sfc}^{net} - SH - LH - G(O). \quad (1)$$

Here, c_s and ρ_s are the effective specific heat capacity and density of the land/ocean surface layer, T_{sfc} is the land/ocean surface temperature (different from the surface air temperature T), R_{sfc}^{net} is the net radiation absorbed by the land/ocean surface, SH and LH are the surface sensible and latent heat fluxes (positive upward), and G represents conduction of heat to deeper soil layers (positive downward) or ocean heat-uptake O. In equilibrium states, the temperature tendency and the uptake term G/O can be neglected, leaving the approximate balance (see more in Figure S5)

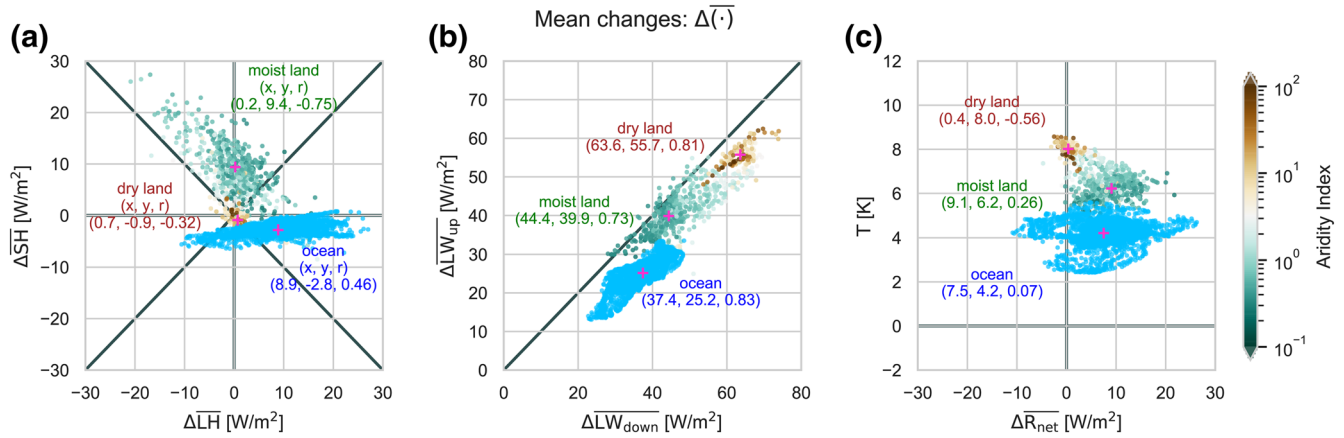

Figure 2. Paired summer-mean changes in (a) sensible heat (SH) flux and latent heat (LH) fluxes, (b) upwelling and downwelling longwave radiation (LW_{up} and LW_{down}) at the surface, and (c) surface air temperature (T) and net radiation flux (R_{net}) at the surface. Each dot represents one grid cell, including all land (shaded according to base-climate summer-mean Aridity Index) and ocean (shaded in sky blue) grid cells within 30°S-30°N. The three pink cross signs in each panel illustrate paired mean values for grid points over dry land (AI ≥ 10), moist land (AI ≤ 1), and ocean. The mean value and the correlation between the paired variables for grid points over the three surface types are also annotated.

$$SH + LH \approx R_{sfc}^{net}. \quad (2)$$

The Bowen ratio, $\mathcal{B}$ = SH / LH, tracks partitioning between the surface sensible and latent heat fluxes under this energy balance constraint. This partitioning is important because SH directly impacts surface air temperature whereas LH does not.

Figure 2 illustrates paired changes between the control climate and the warm climate in selected summer-mean surface variables. Since most of the consistent and pronounced signals of the upper tail amplification (red shading in Figure 1c) appear in the tropics and the subtropics, we focus on 30°S-30°N to analyze changes of the underlying surface fluxes. Including land grid cells within 60°S-60°N yields similar results.

Dry land grids (brown dots) show small changes in both SH and LH (mean changes less than 1 W/m^2), while moist land regions (green dots) show a negative correlation (r = –0.75) between SH and LH (Figure 2a). For the latter regions, almost all grid cells show increases in SH while some show increases and others decreases in LH. This indicates that turbulent flux (SH + LH) is partitioning toward SH (higher Bowen ratio), though LH (evapotranspiration) is not necessarily reduced. Over the ocean (blue dots), LH increases for most of the grid points (an average of 9 W/m^2) while SH decreases (an average of −3 W/m^2), indicating a lower Bowen ratio in warmer climate.

Relative to wet surfaces, dry surfaces show larger increases in both LW_{up} and LW_{down} under the 4 × CO_2 equilibrium (Figure 2b). Changes in these two fluxes generally follow a nearly 1:1 relationship. However, LW_{down} tends to increase slightly more than LW_{up}, especially over oceanic and dry land surfaces, implying an increase in net longwave radiation (LW_{net}) absorbed at the surface. Increases in LW_{up} can be attributed to increases in (land/ocean) surface temperature, while increase in LW_{down} can be attributed to increases in lower-layer air temperature and greenhouse gas concentrations. Increases in near-surface CO_2 and specific humidity imply a downward shift in the effective emission level for LW_{down}, toward warmer temperatures. As a result, LW_{down} may be expected to increase more than LW_{up} even given equal increases in surface temperature and lower-layer air temperature. This appears to be the case for grid points over the dry land. For the ocean, the decrease in SH implies that sea surface temperature increases slightly less than the air temperature above, further damping the increase in LW_{up} relative to LW_{down}. Over moist land surfaces, increases in SH and roughly similar increases in LW_{down} and LW_{up} are both consistent with land surface temperature warming more than the air temperature above.

Net radiation (including both LW and solar fluxes) absorbed at the surface increases more over wet surfaces than over dry surfaces, while temperature increases more over dry land regions (Figure 2c). Counter-in-

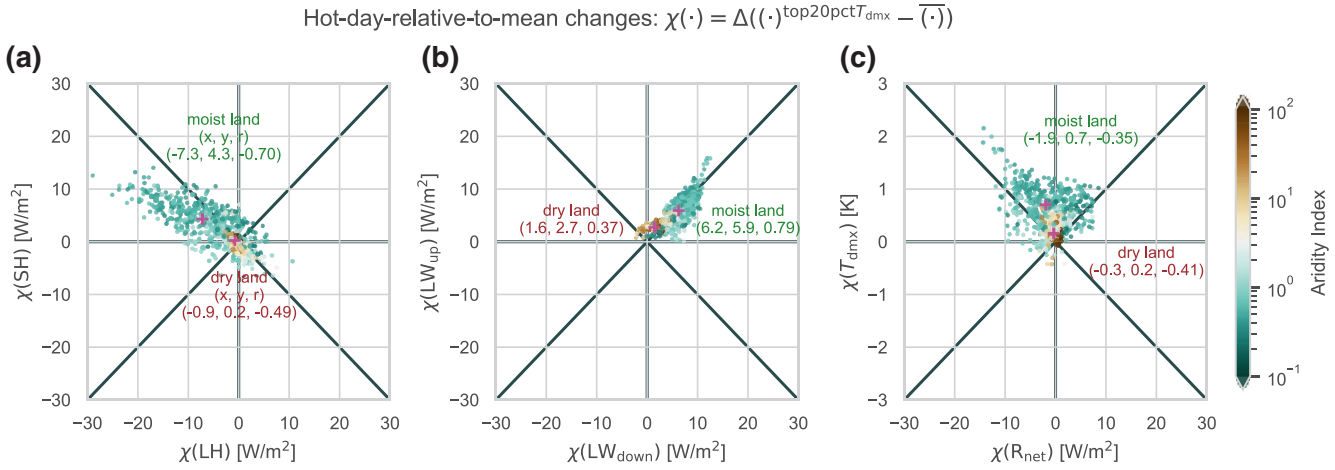

Figure 3. Same as in Figure 2, but for conditions in extreme hot days relative to the mean state. Land grid cells within 30°S-30°N are plotted. Ocean grid cells are omitted.

tuitively, changes in surface air temperature do not have strong positive correlation with changes in net radiation. A perspective worth-mentioning is that, the changes in surface fluxes in Figure 2 are differences between two equilibrium states. They are "end-results" of the temperature and atmospheric composition change from the base climate to the warm climate, rather than "drivers" of the temperature change.

Changes in summer-mean T and surface fluxes can thus be summarized as follows:

- The dry regime reaches its new equilibrium with little change in summer-mean SH or net radiation, indicating that surface temperature and surface air temperature warm by roughly equal amounts. The new equilibrium state is reached with compensating adjustments among the components radiative fluxes. Limited surface moisture leaves LH little freedom to change under the dry regime.
- The oceanic regime has no such limitation, allowing more flexibility for LH to increase. Indeed, LH increases significantly to balance an increase in net radiation received at the surface. SH decreases slightly in this regime, and the Bowen ratio becomes lower.
- The moist land regime differs from the dry regime in that the new equilibrium is not reached with compensating adjustments in downwelling and upwelling radiation. It also differs from the oceanic regime in that surface moisture supplies are more limited. As a result, both SH and LH adjust to balance the additional net radiation received at the surface. The mean Bowen ratio generally increases, though LH does not necessarily decrease.

We show in the following subsection that this mean-state change differs from changes on extreme hot days, when the moist land regime becomes more water-limited and LH (evapotranspiration) decreases more severely.

3.3. Warming of the Extreme

Figure 3 shows the anomalous changes in surface fluxes and temperature on summertime extreme hot days relative to changes in the mean state. Surface SH, LH, and radiation fluxes are composited on T_{dmx}.

Results for dry land regions consistently cluster near the origin, indicating that these regions exhibit no obvious amplification in changes of either extreme temperature or associated surface fluxes. The distribution of T_{dmx} and related surface energy fluxes shift in tandem with the mean state under global warming, with little elongation of the "hot tail."

Over moist land regions, we find a strong anticorrelation (r = –0.7) between SH and LH (Figure 3a). For most locations, extreme hot days are characterized by amplified increases in SH and amplified decreases

in LH. Negative changes in LH are more ubiquitous for changes in extreme hot days than mean state (Figure 2a). These results imply that suppressed evapotranspiration during heatwave events further partitions the surface turbulent flux toward SH, amplifying increases in the Bowen ratio and exacerbating warming on the hottest days. Corresponding changes in LW_{up} and LW_{down} are positively correlated and closely follow the 1:1 line, with larger changes for smaller values of the climatological AI in general (Figure 3b). The dependence on the AI is opposite to that found for the mean state (Figure 2b), consistent with simulated extreme-relative-to-mean changes being most pronounced for climatologically moist land regions. There are a handful of dots with very small climatological AI values (very moist) located very close to the origin—these are grid cells along the southern edge of the Tibetan plateau. High orographic precipitation rates simulated in these regions lead to very small AI values, but the land surface properties there differ from the typical tropical/subtropical moist land.

Net radiation changes are near zero for dry land regions and slightly negative on average for moist land regions (Figure 3c), although the latter exhibits a large spread that includes both positive and negative values. As for changes in the mean state, increases in temperature on the hottest days do not show apparent positive correlation with changes in net radiation.

4. Discussion: Suppressed Evapotranspiration Exacerbates Warming

Warming in both the mean and the extreme is greater over land than over ocean. Current arguments for this amplified warming over land include larger lower-tropospheric temperature lapse rates over land than over ocean (including later refinements of this idea based on convective quasiequilibrium and weak-free tropospheric temperature gradient; Byrne & O'Gorman, 2013, 2016, 2018; Joshi et al., 2008), and land surface feedbacks involving soil moisture or vegetation responses to climate change (e.g., Berg et al., 2016; Donat et al., 2017; Fischer et al., 2007; Jaeger & Seneviratne, 2011; Lemordant & Gentine, 2018; Lorenz et al., 2016). The former was used to compare mean equilibrium states, and in this framework the key control of amplified warming over land is the boundary-layer relative humidity, which determines the lifted condensation level above which the lapse rate is reduced due to latent heat release. The latter was applied to both mean equilibrium states and transient states (extreme hot days), and in this latter framework the key control of amplified warming is the surface water availability, which determines the Bowen ratio and thereby SH which directly contributes to the boundary-layer heating. Here, we focus more on the latter and compare its roles in both mean-state and extreme-day warming.

Figure 4 shows spatial distributions of changes in summer-mean T, SH, and LH over land (Figures 4a–4c) along with corresponding changes for extreme days relative to the mean state (Figures 4d–4f). For the mean, we find general increases in SH and Bowen ratio over relatively moist tropical and subtropical land areas. However, suppression of evapotranspiration (decreases in LH) is neither widespread nor particularly severe. For extreme-relative-to-mean changes, amplified warming over moist land areas is strongly associated with amplified increases in SH (spatial correlation within 30°S-30°N is 0.66) and amplified decreases in LH (spatial correlation within 30°S-30°N is −0.69). These signals indicate that 40%–50% of the variance in amplified extreme warming over tropical land areas can be explained by enhanced partitioning of surface energy flux toward SH.

For a more quantitative estimate, we can use the results shown in Figures 4d–4f to relate a 1 K amplification (i.e., $\Delta\left(T_{\mathrm{dmx}}^{\mathrm{top20pct}} - \overline{T_{\mathrm{dmx}}}\right) = 1$ K) to an 8 W m^{-2} increase in SH. This value is consistent with the amount of energy needed to heat a 1-km deep layer of boundary-layer air at a rate of 1 K d^{-1}. It is also consistent with the SH feedback parameter calculated from a theoretical equilibrium model of boundary-layer air over land (Cronin, 2013), although this equilibrium framework does not directly extend to the transient hot days as defined here.

The most likely explanation for the redistribution of turbulent enthalpy flux from LH to SH during extreme heat events is suppressed evapotranspiration. Suppression of evapotranspiration may arise from reduced evaporation (e.g., drier soil, less vegetation-intercepted water), reduced transpiration (e.g., stomatal closure associated with CO_2 fertilization and/or heat stress), or some combination of the two. As soil and canopy water declines, the surface is less able to release the radiative energy it absorbs (R_{net}) via LH. As a consequence, a greater proportion of the turbulent enthalpy flux is released via SH.

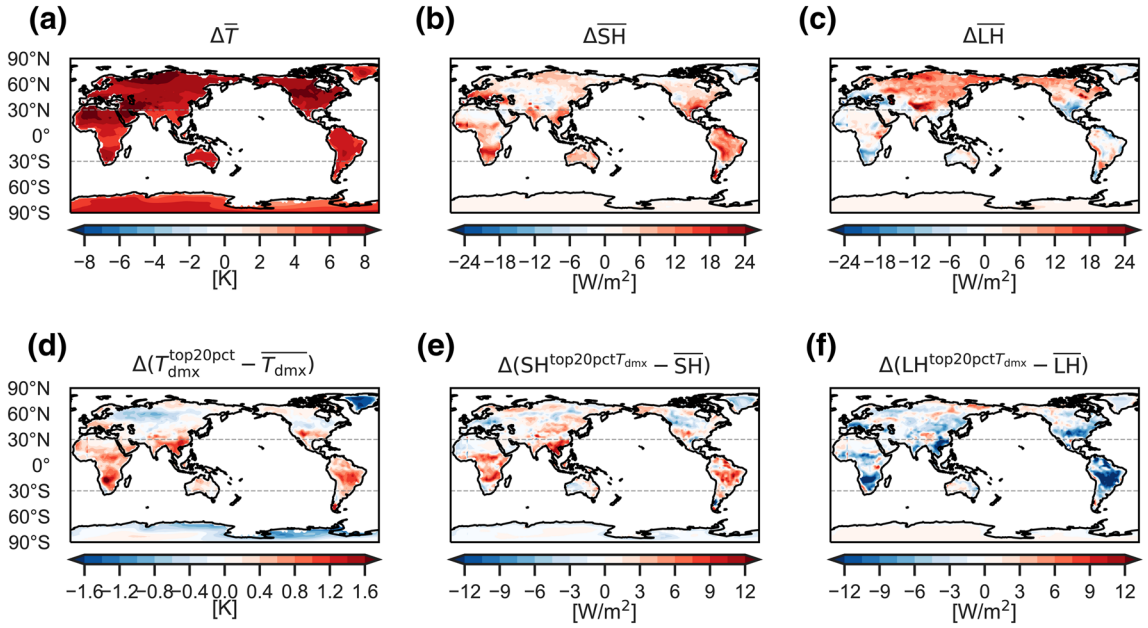

Figure 4. Upper row: spatial patterns of changes in summer-mean (a) temperature, (b) sensible heat flux (SH), and (c) latent heat flux (LH) over land regions. Lower row: spatial patterns of changes on the hottest days $T_{dmx}^{top20pct}$ relative to changes in summertime mean T_{dmx} (d), and corresponding changes in SH (e) and LH (f).

The apparent importance of suppressed evapotranspiration can also explain why the amplification of warming in the extreme (Figures 1c and 4d) emerges mainly over moist land regions. For the warming of extreme events to be substantially amplified relative to the mean warming, the local surface energy balance must be sensitive to fluctuations in moisture availability. In other words, the surface must have sufficient moisture to support strong evapotranspiration fluxes in the mean state; flux partitioning at such surfaces is sensitive to drying or stress-related stomatal closure, leading to suppressed evapotranspiration and larger Bowen ratios on extreme days. In the oceanic regime, the moisture pool is effectively infinite and the surface is not subject to drying, so that surface moisture supply places no comparable constraint on evaporation. Conversely, in the dry regime, the surface mean state is already dry, reducing potential differences in evapotranspiration between the mean state and extreme events. Therefore, elongation of the upper tail of summer temperature distribution is distinctive to moist land regions, where surface moisture supplies are both relatively plentiful and can vary substantially in time.

5. Summary and Outlook

We compare patterns of summertime mean warming and warming associated with the hottest summertime daily maximum temperatures (Figure 1). We find that dry and wet surfaces experience different changes in mean and extreme regions of the temperature distribution, which we classify into three distinct regimes:

- Dry land regime: the entire temperature distribution is shifted, with pronounced warming in the mean state and little amplification in the tail relative to the mean.
- Moist land regime: mean warming is smaller than the dry land regime, but warming of extreme hot days is amplified, indicating an elongated upper tail of the temperature distribution. This amplification (Figure 1c) is compounded on top of the land-ocean contrast in mean warming (Figure 1a), and reaches magnitudes as large as 20% of the global mean warming.
- Oceanic regime: mean warming is weaker than over land surfaces, with no evident change in the length of the upper tail.

Adjustment of the surface flux balance differs among these three regimes. In the dry land regime there is little change in the turbulent SH or LH fluxes; the additional energy is balanced mainly via radiative flux adjustment. By contrast, in the oceanic regime, the surface turbulent flux partitions toward LH (a smaller

Bowen ratio), while in moist land regime the surface turbulent flux partitions toward SH (a larger Bowen ratio). Increases in the Bowen ratio over moist land regions are even more pronounced on extreme hot days, as suppressed evapotranspiration (which is not evident in the mean state change) amplifies the effects of increased SH. This exacerbation of suppressed evapotranspiration on hot days explains why the amplified warming in the extreme emerges mainly over moist land regions (Figures 1c and 4d): Over moist land, moisture is potentially limited (unlike the ocean) and mean evapotranspiration is large enough that its disruption substantially alters the Bowen ratio (unlike dry land regions).

There remain a number of issues to resolve. Figure 4 shows that the Bowen ratio tends to increase with warming over most tropical and subtropical land regions, but with different quantitative increases between the mean state and the extreme state. When and why is surface evapotranspiration suppressed? Is this suppression typically rooted in local soil moisture, vegetation, or radiation responses? Early results indicate that the answers to these questions vary considerably across locations and models. A detailed analysis is therefore needed to identify a generalizable framework for understanding the contributions of surface drying to heat events over different surface types in a warmer world.

Data Availability Statement

CMIP5 model outputs used in this study are downloaded from CMIP5 data archive (https://cmip.llnl.gov/cmip5/), as well as CEDA data archive (http://data.ceda.ac.uk/badc/cmip5/data/cmip5/output1/). The authors appreciate institutions that generate and host these data.

Acknowledgments
The authors thank Prof. Stephan Fueglistaler and Prof. David Romps for providing guidance and insights at different stages of this project. The authors also thank Dr. Khaled Ghannam, Dr. Yujin Zeng, and Dr. Zhihong Tan for helpful prereviews of the paper. The authors appreciate helpful comments and suggestions from two anonymous reviewers. The authors acknowledge support from National Science Foundation Awards (NSF PIRE-1743753), and the grant from the Ministry of Science and Technology of the People's Republic of China to Tsinghua University (2017YFA0603902).

References

Ballester, J., Giorgi, F., & Rodo, X. (2010). Changes in European temperature extremes can be predicted from changes in PDF central statistics. *Climatic Change*, *98*(1–2), 277. https://doi.org/10.1007/s10584-009-9758-0

Berg, A., Findell, K., Lintner, B., Giannini, A., Seneviratne, S. I., Van den Hurk, B., et al. (2016). Land-atmosphere feedbacks amplify aridity increase over land under global warming. *Nature Climate Change*, *6*(9), 869–874. https://doi.org/10.1038/nclimate3029

Byrne, M. P., & O'Gorman, P. A. (2013). Land-ocean warming contrast over a wide range of climates: Convective quasi-equilibrium theory and idealized simulations. *Journal of Climate*, *26*(12), 4000–4016. https://doi.org/10.1175/JCLI-D-12-00262.1

Byrne, M. P., & O'Gorman, P. A. (2016). Understanding decreases in land relative humidity with global warming: Conceptual model and GCM simulations. *Journal of Climate*, *29*(24), 9045–9061. https://doi.org/10.1175/JCLI-D-16-0351.1

Byrne, M. P., & O'Gorman, P. A. (2018). Trends in continental temperature and humidity directly linked to ocean warming. *Proceedings of the National Academy of Sciences*, 201722312, *115*(19), 4863–4868. https://doi.org/10.1073/pnas.1722312115

Chan, D., Cobb, A., Zeppetello, L. R. V., Battisti, D. S., & Huybers, P. (2020). Summertime temperature variability increases with local warming in midlatitude regions. *Geophysical Research Letters*, *47*(13), e2020GL087624. https://doi.org/10.1029/2020GL087624

Clark, R. T., Brown, S. J., & Murphy, J. M. (2006). Modeling northern hemisphere summer heat extreme changes and their uncertainties using a physics ensemble of climate sensitivity experiments. *Journal of Climate*, *19*(17), 4418–4435. https://doi.org/10.1175/JCLI3877.1

Cronin, T. W. (2013). A sensitivity theory for the equilibrium boundary layer over land. *Journal of Advances in Modeling Earth Systems*, *5*(4), 764–784. https://doi.org/10.1002/jame.20048

Della-Marta, P. M., Haylock, M. R., Luterbacher, J., & Wanner, H. (2007). Doubled length of western European summer heat waves since 1880. *Journal of Geophysical Research*, *112*, D15103, https://doi.org/10.1029/2007JD008510

Diffenbaugh, N. S., & Ashfaq, M. (2010). Intensification of hot extremes in the United States. *Geophysical Research Letters*, *37*(15), L15701. https://doi.org/10.1029/2010GL043888

Diffenbaugh, N. S., & Charland, A. (2016). Probability of emergence of novel temperature regimes at different levels of cumulative carbon emissions. *Frontiers in Ecology and the Environment*, *14*(8), 418–423. https://doi.org/10.1002/fee.1320

Diffenbaugh, N. S., & Scherer, M. (2011). Observational and model evidence of global emergence of permanent, unprecedented heat in the 20th and 21st centuries. *Climatic Change*, *107*(3–4), 615–624. https://doi.org/10.1007/s10584-011-0112-y

Diffenbaugh, N. S., Singh, D., Mankin, J. S., Horton, D. E., Swain, D. L., Touma, D., et al. (2017). Quantifying the influence of global warming on unprecedented extreme climate events. *Proceedings of the National Academy of Sciences*, *114*(19), 4881–4886. https://doi.org/10.1073/pnas.1618082114

Donat, M. G., & Alexander, L. V. (2012). The shifting probability distribution of global daytime and night-time temperatures. *Geophysical Research Letters*, *39*(14), L14707. https://doi.org/10.1029/2012GL052459

Donat, M. G., Pitman, A. J., & Seneviratne, S. I. (2017). Regional warming of hot extremes accelerated by surface energy fluxes. *Geophysical Research Letters*, *44*(13), 7011–7019. https://doi.org/10.1002/2017GL073733

Fischer, E. M., Beyerle, U., & Knutti, R. (2013). Robust spatially aggregated projections of climate extremes. *Nature Climate Change*, *3*(12), 1033–1038. https://doi.org/10.1038/nclimate2051

Fischer, E. M., & Schär, C. (2009). Future changes in daily summer temperature variability: Driving processes and role for temperature extremes. *Climate Dynamics*, *33*(7–8), 917. https://doi.org/10.1007/s00382-008-0473-8

Fischer, E. M., Seneviratne, S. I., Lüthi, D., & Schär, C. (2007). Contribution of land-atmosphere coupling to recent European summer heat waves. *Geophysical Research Letters*, *34*(6), L06707. https://doi.org/10.1029/2006GL029068

Gentine, P., D'Odorico, P., Lintner, B. R., Sivandran, G., & Salvucci, G. (2012). Interdependence of climate, soil, and vegetation as constrained by the Budyko curve. *Geophysical Research Letters*, *39*(19), L19404. https://doi.org/10.1029/2012GL053492

Gross, M. H., Donat, M. G., Alexander, L. V., & Sisson, S. A. (2018). The sensitivity of daily temperature variability and extremes to dataset choice. *Journal of Climate*, *31*(4), 1337–1359. https://doi.org/10.1175/JCLI-D-17-0243.1

Hansen, J., Sato, M., & Ruedy, R. (2012). Perception of climate change. *Proceedings of the National Academy of Sciences*, *109*(37), E2415–E2423. https://doi.org/10.1073/pnas.1205276109

Jaeger, E. B., & Seneviratne, S. I. (2011). Impact of soil moisture-atmosphere coupling on European climate extremes and trends in a regional climate model. *Climate Dynamics*, *36*(9–10), 1919–1939. https://doi.org/10.1007/s00382-010-0780-8

Joshi, M. M., Gregory, J. M., Webb, M. J., Sexton, D. M., & Johns, T. C. (2008). Mechanisms for the land/sea warming contrast exhibited by simulations of climate change. *Climate Dynamics*, *30*(5), 455–465. https://doi.org/10.1007/s00382-007-0306-1

Kodra, E., & Ganguly, A. R. (2014). Asymmetry of projected increases in extreme temperature distributions. *Scientific Reports*, *4*, 5884. https://doi.org/10.1038/srep05884

Lemordant, L., & Gentine, P. (2018). Vegetation response to rising CO_2 impacts extreme temperatures. *Geophysical Research Letters.46*(3), 1383–1392. https://doi.org/10.1029/2018GL080238

Lorenz, R., Argiieso, D., Donat, M. G., Pitman, A. J., Van den Hurk, B., Berg, A., et al. (2016). Influence of land-atmosphere feedbacks on temperature and precipitation extremes in the GLACE-CMIP5 ensemble. *Journal of Geophysical Research: Atmosphere*, *121*(2), 607–623. https://doi.org/10.1002/2015JD024053

McKinnon, K. A., Rhines, A., Tingley, M. P., & Huybers, P. (2016). The changing shape of northern hemisphere summer temperature distributions. *Journal of Geophysical Research: Atmosphere*, *121*(15), 8849–8868. https://doi.org/10.1002/2016JD025292

Milly, P. C., & Dunne, K. A. (2016). Potential evapotranspiration and continental drying. *Nature Climate Change*, *6*(10), 946–949. https://doi.org/10.1038/nclimate3046

Rhines, A., & Huybers, P. (2013). Frequent summer temperature extremes reflect changes in the mean, not the variance. *Proceedings of the National Academy of Sciences*, *110*(7), E546. https://doi.org/10.1073/pnas.1218748110

Rhines, A., McKinnon, K. A., Tingley, M. P., & Huybers, P. (2017). Seasonally resolved distributional trends of North American temperatures show contraction of winter variability. *Journal of Climate*, *30*(3), 1139–1157. https://doi.org/10.1175/JCLI-D-16-0363.1

Schär, C., Vidale, P. L., Lüthi, D., Frei, C., Haberli, C., Liniger, M. A., & Appenzeller, C. (2004). The role of increasing temperature variability in European summer heatwaves. *Nature*, *427*(6972), 332–336. https://doi.org/10.1038/nature02300

Sulikowska, A., & Wypych, A. (2020). Summer temperature extremes in Europe: How does the definition affect the results? *Theoretical and Applied Climatology*, *141*, 19–30. https://doi.org/10.1007/s00704-020-03166-8

Taylor, K. E., Stouffer, R. J., & Meehl, G. A. (2012). An overview of CMIP5 and the experiment design. *Bulletin of the American Meteorological Society*, *93*(4), 485–498. https://doi.org/10.1175/BAMS-D-11-00094.1

Tingley, M. P., & Huybers, P. (2013). Recent temperature extremes at high northern latitudes unprecedented in the past 600 years. *Nature*, *496*(7444), 201–205. https://doi.org/10.1038/nature11969

Vogel, M. M., Orth, R., Cheruy, F., Hagemann, S., Lorenz, R., Hurk, B., & Seneviratne, S. I. (2017). Regional amplification of projected changes in extreme temperatures strongly controlled by soil moisture-temperature feedbacks. *Geophysical Research Letters*, *44*(3), 1511–1519. https://doi.org/10.1002/2016GL071235

Wang, L., Huang, J., Luo, Y., Yao, Y., & Zhao, Z. (2015). Changes in extremely hot summers over the global land area under various warming targets. *PLoS ONE*, *10*(6), e0130660. https://doi.org/10.1371/journal.pone.0130660